Flushing time variability in a short, low-inflow estuary

Mohsen Taherkhani[1], Sean Vitousek[2,6], Ryan K. Walter[3], Jennifer O'Leary[4,5], and Amid P. Khodadoust[6]

[1]Civil and Construction Engineering Department, Oregon State University, Corvallis, OR, USA
[2]United States Geological Survey, Pacific Coastal and Marine Science Center, Santa Cruz, CA, USA
[3]Physics Department, California Polytechnic State University, San Luis Obispo, CA, USA
[4]California Sea Grant, San Luis Obispo, CA, USA
[5]Wildlife Conservation Society, Mombasa, Kenya
[6]Civil, Materials, and Environmental Engineering Department, University of Illinois at Chicago, Chicago, IL, USA

Abstract

Flushing time, the time scale for exchange and mixing between embayed and oceanic waters in an estuary, plays an integral role in determining water quality and aquatic ecosystem health. Here, we investigated the spatiotemporal variability of flushing times throughout Morro Bay, a short, low-inflow estuary (LIE) on the California coast, using a calibrated and validated hydrodynamic model (Delft3D). Morro Bay has historically supported an extensive eelgrass (*Zostera marina*) habitat, which declined substantially from 139 ha to 5.4 ha during 2007-2017. Eelgrass decline motivated the current research into the role of changing bed roughness and oceanic drivers (i.e., tide and sea-level rise) on estuarine hydrodynamics and flushing times. We found that tidal variability exerts the strongest control on flushing times compared to other effects like bed roughness or sea-level rise. Additionally, we found that increasing sea level and decreasing bed roughness (associated with declining seagrass coverage) yielded higher rates of mixing (lower flushing times). We detected a strong correspondence between areas having shorter flushing times (e.g., near the estuary mouth) and areas occupied by resilient eelgrass populations in Morro Bay. Our findings further indicate that flushing times in short LIEs are particularly sensitive to several factors (e.g., bed roughness, sea level) that are susceptible to anthropogenic disturbance and future climate change.

1. Introduction

Flushing time is a critical metric for water quality and aquatic ecosystem health (Sanford et al., 1992). Estuarine flushing time, the time scale for partial or complete exchange and mixing of embayed and oceanic waters in an estuary, directly affects water quality by controlling the residence time of oceanic and terrestrial waters within a defined boundary (den Heyer & Kalff, 1998; Dettmann, 2001; Hamilton & Lewis Jr., 1987; Monsen et al., 2002; Nixon et al., 1996). The distribution and persistence of nutrients, contaminants, dissolved gases, and suspended

particles in estuarine systems are primarily affected by estuarine flushing times (Dettmann, 2001; Josefson & Rasmussen, 2000). Moreover, estuarine flushing times are strongly driven by several oceanic and hydrodynamic processes (e.g., Huggett et al., 2021). Yet, few studies have investigated the specific processes responsible for spatiotemporal variability in flushing times in estuarine systems despite their implications for water quality and resilience of estuarine ecosystems.

Estimates of flushing time are typically derived from the time it takes for tracers (in the form of passively advected scalars or tracked particles) initialized at a specific location to exchange out of a domain by currents (e.g., Cucco et al., 2009). Thus, flushing time is considered a bulk or integrative parameter that describes general exchange without explicit consideration of the contributions from individual hydrodynamic processes or their spatiotemporal distribution (Monsen et al., 2002). The underlying hydrodynamics that drive coastal and estuarine circulation (and thus flushing time) are highly variable in space and time and are sensitive to factors including physical forcings (e.g., tides, winds, freshwater inputs), geomorphology (e.g., bed roughness), and geometry (e.g., length, width, and water depth). A limited number of recent studies attempted to quantify the relative influence of some of these factors on estuarine flushing time (e.g., Andutta et al., 2013; Hinrichs et al., 2018; Jiang et al., 2019), but these studies were mainly limited to estuaries with persistent freshwater inflow. In low-inflow estuaries (LIEs), transport and exchange between the estuary and ocean are primarily controlled by tidal diffusion since freshwater inputs are inadequate to stratify the estuaries during large portions of the year, in contrast to high-inflow ("classical") estuaries with enhanced two-layer gravitational circulation (Largier, 2010; Largier et al., 1997; MacCready & Geyer, 2010; Walter et al., 2018). Weak tidal mixing near the head of a LIE can lead to increased flushing times and the development of significant differences in water properties and ecosystem habitats (Buck et al., 2014; Largier, 2010; Walter et al., 2018; Wilson et al., 2021). Due to their weak exchange (e.g., due to lack of a persistent inflow/outflow) and relatively long flushing times, LIEs are particularly sensitive to changes in climate (e.g., wet and dry years) and human disturbance (e.g., dredging, estuary modification, eutrophication, etc.) and may require more proactive management strategies (Schettini et al., 2017) that would benefit from information on flushing time and its relationship with estuarine water quality.

In short and shallow estuarine systems, tidal hydrodynamics are sensitive to changes in water depth, bed roughness, geometry, and anthropogenic activities that modify these properties (Khojasteh et al., 2021; Ralston et al., 2019; Talke & Jay, 2020). Relative sea level also alters tidal dynamics by changing the water depth, tidal velocities, and tidal range (Holleman & Stacey, 2014; Sinha et al., 1997; Zhong et al., 2008). Recent numerical simulations show that flushing time and tidal exchange volume are inversely proportional (Rynne et al., 2016; Xiong et al., 2021). Shallow systems are susceptible to changes in tidal amplitude since small increases in depth can result in relatively significant decreases in effective friction (Talke & Jay, 2020). Likewise, friction and bed roughness in shallow estuarine systems are modified by the presence of aquatic vegetation like seagrasses, which influence hydrodynamics by increasing drag on the flow and damping near-bed velocities and wave energy (Horstman et al., 2013; Kobashi & Mazda, 2005; Lacy & Wyllie-Echeverria, 2011; Luhar et al., 2010; Luhar & Nepf, 2013; Nepf, 2012). Amid a global decline in seagrass systems (Waycott et al., 2009), it is crucial to investigate how habitat loss alters bed roughness, circulation patterns, and flushing times,

leading to potential feedbacks to the hydrodynamics of estuarine systems. This is especially important in shallow systems where the fraction of the water column occupied by drag elements (e.g., seagrasses or other biogenic habitats) is larger compared to deeper systems. As a result, for the same flow, a shallower system will produce more drag and yield an increased effective bed roughness compared to a deeper system (McDonald et al., 2006; Monismith et al., 2019).

In this study, we investigated the spatiotemporal variability of flushing times in Morro Bay, a short, seasonally LIE that has historically supported an important seagrass habitat and is located along the central California coast. To better understand how hydrodynamic processes in the estuary influence estuarine health and seagrass habitats, we developed a hydrodynamic numerical model (Delft3D), which was calibrated and validated using in-situ observations. We then assessed the sensitivity of flushing time estimates throughout the estuary to changes in factors that influence local hydrodynamics, including tidal variability/range, bed roughness [to simulate bed conditions before and after the eelgrass decline despite the caveat that changing vegetation characteristics are subject to more complexities than just altered bed roughness (Dijkstra & Uittenbogaard, 2010)], and projected future sea-level rise. Our findings provide context for understanding the flushing times of LIEs globally with potential implications for the management of LIE ecosystems.

2. Study Site

Morro Bay is a short and shallow estuary on the central coast of California, U.S. (Figure 1a). It is part of the National Estuary Program (NEP) and supports diverse wildlife, including invertebrates, fish, and native and migrating bird populations. The main channel runs along the length of the estuary (~6.5 km long) and gets progressively shallower and narrower going from the mouth (~10 m depth) to the head of the bay (Figure 2). The main channel is flanked by expansive intertidal mudflats, historically supporting one of the state's largest eelgrass (Zostera marina) populations (Figure 1b) and representing the estuary's major benthic habitat. Morro Bay is characterized by a Mediterranean climate with an extended dry summer season (~April to October), with little to no precipitation and freshwater inflows. In contrast, during the shorter wet winter season (~November to March), the estuary receives episodic rainfall and freshwater inflows, with considerable interannual variability during the wet season (see e.g., Figure 2 in Walter et al., 2020). We focus on the dry summer season dynamics in this contribution. Like other US West Coast estuaries, Morro Bay has mixed semi-diurnal tides (with a mean tidal range of ~1.09 m and a significant diurnal range of ~1.62 m based on the nearby tide station at Port San Luis, CA).

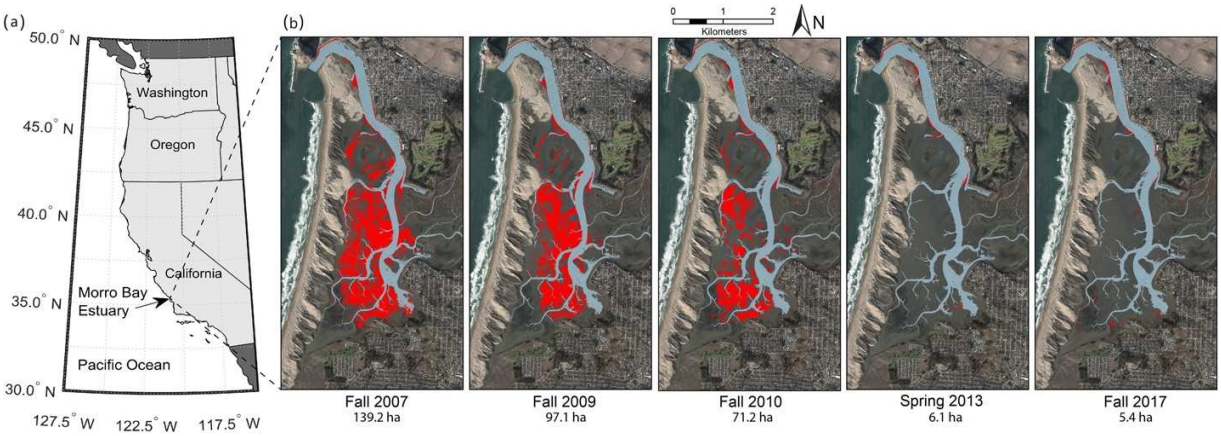

Figure 1. *(a) Location of Morro Bay on the Central Coast of California. (b) The spatial distribution of eelgrass coverage over time from 2007 to 2017 highlighting the period of major decline, where red areas represent eelgrass extent, and grey areas show the extent of the subtidal channels. [Modified from Walter et al. (2020)]*

Over a decade, intertidal eelgrass in Morro Bay underwent an unprecedented loss, declining from 139.2 ha (344 acres) in 2007 to 5.4 ha (13 acres) in 2017 (Harenčár et al., 2018; O'Leary et al., 2021; Walter et al., 2018, 2020). The majority of eelgrass losses occurred from 2010 to 2013 in the intertidal flats in the mid- to back-bay (Figure 1b). Research following the decline has documented changes in fish populations and declines in species that require eelgrass habitat (O'Leary et al., 2021), decreases in migratory Brant geese numbers, and widespread erosion in places that previously supported vibrant eelgrass populations (Walter et al., 2020). While the cause of the decline is still unclear, recent research after the decline showed that there are strong gradients in environmental conditions (e.g., hydrodynamic state variables such as density and temperature, as well as water quality parameters like turbidity and dissolved oxygen, that, in turn, can generate gradients in eelgrass health and survival) throughout the bay (Walter et al., 2018). Moreover, it remains unknown how the decline in eelgrass might affect bed roughness, hydrodynamic conditions, and other water quality parameters throughout the bay (see also Bartoloni et al., 2023). Recent drone-based surveys throughout the bay from Dec 2017 to Dec 2020 showed an unexpected reemergence of eelgrass throughout portions of the bay, with acreage going from 5.4 ha (13.3 acres) to 6.6 ha (16.4 acres) to 14.9 ha (36.7 acres) to 59.4 ha (146.9 acres) in 2017, 2018, 2019, and 2020, respectively, suggesting that Morro Bay may be going through another major period of transition and possible restoration of the major biogenic habitat.

3. Materials and Methods

3.1. Data Collection

Oceanographic moorings were deployed throughout the estuary during the summer 2018 dry season to help calibrate and validate the numerical model. These moorings were deployed from Jul 31st, 2018, to Sept 3rd, 2018, at four sites along the main channel (Figure 2a), including at the mouth (BM), near the center (BC), towards the back center near oyster farms (BO), and at the far south end of the bay near the head (BS). Water velocities were measured using bottom-mounted

current meters (with transducers all located approximately 0.5 m from the bed) at all sites except BS, which was too shallow to allow for accurate current measurements given instrument blanking distances and surface layer effects. Currents at BM were measured with a Teledyne RDI Sentinel V20 acoustic Doppler current profiler (2 s sampling rate with 10 min averages and 0.3 m vertical bin size), while currents at BC and BO were measured using a 2.0 MHz Nortek acoustic Doppler profiler (1 s sampling rate with 10 min averages and 0.3 m vertical bin size). All current meters were leveled by divers to within 1° of the horizontal to minimize instrument tilt errors, and surface layer effects were removed based on echo intensity values (typically top 10% of the water column). Due to high biofouling rates and drifting macroalgae that can accumulate on sensors in previous deployments, sensors were checked and cleaned approximately weekly by divers. In addition to current meters, all sites also had Sea Bird Electronics 37 SMP conductivity-temperature-depth (CTD) sensors fixed on moorings at 2 meters above the bed (mab). The 2 mab sensors at BM, BC, and BO sampled every 150 s and had optical dissolved oxygen sensors (SBE 63; not used in this study), while the 2 mab sensor at BS sampled at 15 s intervals. All times referenced are in local time (Pacific Daylight Time).

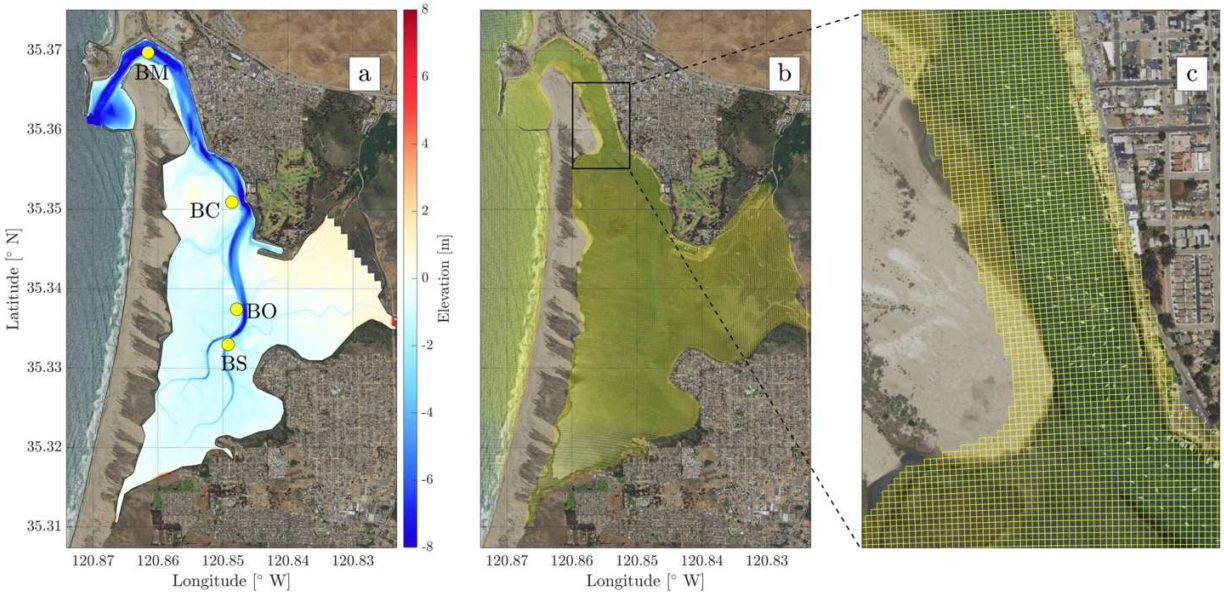

Figure 2. *(a) Morro Bay bathymetry, where the yellow dots represent the location of monitoring stations. (b) The bathymetric grid system implemented in the model highlighting the higher resolution on the subtidal and intertidal portions of the estuary. (c) A selected portion of the entrance channel depicting grid resolution as fine as 10 m grid size.*

3.2. Numerical Model

3.2.1. Model Configuration and Calibration

We simulated the hydrodynamics in Morro Bay using Delft3D (Roelvink & Van Banning, 1995), a modeling system that has widespread applicability to flows in shallow coastal regions (Lesser et al., 2004). Delft3D has also been shown to be well-suited to simulate shallow estuarine environments and flushing times (Al-Asadi & Duan, 2017; Andutta et al., 2016; Christensen et

al., 2020; Horstman et al., 2013; Leijnse et al., 2021; Mariotti & Murshid, 2018; Palazzoli et al., 2020; Pokavanich & Alosairi, 2014; Rynne et al., 2016; Sullivan et al., 2020). For computational efficiency, we employed a two-dimensional (2D) depth-averaged model since Morro Bay is shallow, and strong tidal mixing leads to unstratified conditions during the summer, low-inflow period (the focus of this study). The use of a 2D model is justified given the negligible stratification observed along the main channel of Morro Bay during the same time period (see Figure S2 Bartoloni et al. 2023 for CTD casts during this experiment) and lack of baroclinicity in vertical profiles of currents measured.

The model domain encompasses all the areas inside Morro Bay that are submerged during spring high tides, extending to approximately 3 km offshore of the bay mouth (Figure 2b). The Delft3D (curvilinear) grid used in the current study was adapted from grid files developed by the U.S. Geological Survey (USGS) for Morro Bay as part of the Coastal Storm Modeling System (CoSMoS) project (Barnard et al., 2014). The original CoSMoS grid was modified and refined by substantially increasing the grid resolution inside the bay and at the mouth. (Figure 2b, c). The modified grid system has approximately 77,000 grid cells. The grid resolution is approximately 10 m inside the bay, with higher resolution (e.g., ~5 m) in some locations along the central, intertidal portions of the bay.

The bathymetry dataset used in this study was collected by NOAA during the spring and early summer of 2019 (https://inport.nmfs.noaa.gov/inport/item/57916), which is the most current bathymetry data available for the numerical simulation period. This product is a 1 m resolution Digital Elevation Model (DEM) combining aerial LiDAR (Light Detection and Ranging) and multibeam acoustic bathymetric data. This dataset uses the North American Datum of 1983 (NAD83) as the horizontal datum and the mean sea level (MSL) as the vertical datum.

Delft3D solves the nonlinear shallow-water equations using the finite-difference method and computes primary hydrodynamic variables (e.g., water level, velocities, temperature, etc.) at each computational grid cell using user-defined bathymetry, bed roughness, and horizontal eddy viscosity and diffusivity. In the current application, we included the model processes of temperature, salinity, and the concentration of a passively advected and diffused tracer, differentiating water entering the embayment from the oceanic source. By tracking the pseudo-concentration of this (unreactive, passive) tracer, we can assess the residence of bay waters as the tracer is mixed with water initially residing in the bay to quantify flushing time. Wind and wave forcing were not included in the model due to Morro Bay's small size and tight enclosure and the dominance of tidal forcing on estuarine circulation (see Walter et al., 2018). Boundary conditions along the ocean-facing perimeter of the model consisted of 118 segments, each with slight variations in tidal amplitude and phase of 13 harmonic constituents, which were obtained from the TPXO 8 global tidal inverse model (Egbert & Erofeeva, 2002). Also, the ocean-facing perimeter temperature boundary conditions are forced by a smoothed (low-pass filtered) temperature signal observed at the mouth of the bay. The water surface temperature boundary condition in the model was calculated via a so-called “excess temperature” heat flux model (Sweers, 1976), which requires the ambient air temperature as its sole boundary condition, here recorded at a nearby meteorological station. No spatial gradients in ambient air temperature nor direct solar radiation boundary conditions are accounted for in this heat-flux method. Yet, no a priori knowledge exists about such temperature gradients or solar radiation forcing throughout

Morro Bay. Thus, the simplistic approach of spatially uniform background temperature is opted here. The model is started from rest (i.e., zero initial velocity) with a uniform water level consistent with the tidal stage. A model time step of 10 seconds was used to maintain numerical stability and accuracy in the simulation, and the model output was saved every 30 minutes of simulation time throughout the entire simulation period (i.e., 37 days, which corresponds to the period of the field experiment described above).

3.2.2. Hydrodynamics Validation

Field observations at each of the four mooring locations (called BM, BC, BO, and BS and shown in Figure 2a) were used to calibrate the numerical model for state variables such as water level, current velocity, and temperature. The model was calibrated by adjusting the bed roughness and horizontal eddy viscosity/diffusivity to best reproduce the tidal stage and currents throughout the bay. Post-calibration, we found optimal values of $65\ m^{\frac{1}{2}}s^{-1}$ (see Section 3.3.2), $1\ m^2s^{-1}$, and $1\ m^2s^{-1}$ for the bed roughness, horizontal eddy viscosity, and diffusivity, respectively.

To calibrate the model, we quantitatively compared the observed (measured) water level, current velocity (both horizontal components), and temperature at the four mooring locations with the simulated values using various statistical metrics described below, including the correlation coefficient (CC), the root-mean-square error ($RMSE$), and the model $Skill$ (Taylor, 2001; Willmott, 1981) defined as:

$$CC = \frac{n\sum xy - (\Sigma x)(\Sigma y)}{\sqrt{n\Sigma x^2} - (\Sigma x)^2 - \sqrt{n\Sigma y^2} - (\Sigma y)^2} \quad (1)$$

$$RMSE = \sqrt{\overline{(x-y)^2}} \quad (2)$$

$$Skill = 1 - \frac{\Sigma|x-y|^2}{\Sigma(|x-\bar{y}| + |y-\bar{y}|)^2}\ , \quad (3)$$

where x represents the observed (measured) variable, y is the modeled variable, n is the number of pairs of compared data points, an overbar represents the mean over time, and where all summations are performed across all data points in time (using linear interpolation to derive model state variables that are coincident in time with observation). These metrics have been used frequently to determine how well a numerical model can reproduce the observed values for selected hydrodynamic parameters at specific locations (Huggett et al., 2021; Mahanty et al., 2016; Sullivan et al., 2020).

3.3. Flushing Time Estimates

Flushing time is generally defined as a bulk or integrative parameter that quantifies the exchange properties of a body of water without identifying the underlying processes responsible or their spatial distribution (e.g., Monsen et al., 2002). Although flushing time is often treated as a bulk

parameter, in the current study, we sought to investigate the influence of different individual processes (i.e., tidal variability, bed roughness, and mean sea level) on the flushing time as well as investigate the spatiotemporal variability of flushing time. We quantified flushing time using an Eulerian method to track the fate of a non-reactive tracer that is passively advected and dispersed throughout the entire model domain. Tracer-based Eulerian approaches represent a suitable mathematical technique to characterize local flushing times, though they do not predict specific tracer transport trajectories (Lucas & Deleersnijder, 2020).

In the model, a passive tracer with an initial concentration of 1 kg/m^3 (100%) is added uniformly across the model domain (see Figure 3c for the tracer's spatial extent), while any incoming flux of water is assigned a boundary condition concentration of zero (0%):

$$\begin{cases} C_0 = 1\,\frac{kg}{m^3}\ (x,y) \in \Omega \\ C\ = 0\,\frac{kg}{m^3}\ (x,y) \in \partial\Omega\ \text{(during inflow)} \end{cases}, \tag{4}$$

where C is the tracer concentration and C_0 is the initial tracer concentration at time $t = 0$, Ω represents the extent of model domain (see Figure 3c), $\partial\Omega$ represents the model domain boundary at the offshore ends, and the pair (x, y) are the horizontal and vertical spatial coordinates, respectively. To quantify the flushing time (T_f) at each grid cell located in Ω, the concept of a remnant function (r) is commonly adopted:

$$r(x,y,t) = \frac{C(x,y,t)}{C_0(x,y)} = C(x,y,t)\,, \tag{5}$$

which effectively normalizes the tracer concentration (Takeoka, 1984). However, specifying an initial tracer concentration of unity automatically ensures that the tracer is automatically normalized. Hence, $r(x,y,t)$ (or $C(x,y,t)$ by their equivalence) represents the remaining fraction of the tracer concentration at time t in each grid cell in the domain of interest. The Eulerian residence time, T_f, can then be defined as:

$$T_f(x,y) = \int_0^\infty r(x,y,t)dt\,, \tag{6}$$

which is based on the general formula for an integral time scale.

In many tidally-influenced bodies of water subject to flushing, a roughly exponential-like decrease has been observed for mass concentration (e.g., C) via tracer experiments and simulations (Lucas & Deleersnijder, 2020). The decreasing tracer concentration is assumed to follow an exponential form since the instantaneous and evenly mixed introduction of the oceanic water tracer with $C = 0$ kg/m^3 into the domain approximates the behavior of the bay to a continuously stirred tank reactor (CSTR) (Monsen et al., 2002), where the tracer concentration at time t is estimated as:

$$C(t) = C_0 e^{-\frac{t}{T_f}}\,. \tag{7}$$

This single-exponential decay, as opposed to a double-exponential decay (see e.g., Defne & Ganju, 2015), has been utilized as the governing function determining the rate of decay of tracer concentrations in recent literature (Cucco et al., 2009; Drouzy et al., 2019; Jiang et al., 2019; Lencart e Silva et al., 2014; Marsooli et al., 2018; Sullivan et al., 2020). By adopting the CSTR approximation, the remnant function can be written as:

$$r(x, y, t) = e^{-\frac{t}{T_f}}. \quad (8)$$

Here, Eq. 7 and Eq. 8 satisfy the general definitions of remnant function (Eq. 5) and flushing time (Eq. 6) under CSTR conditions. Note that integrating Eq. 8 from time zero to infinity returns a value of T_f , which is consistent with the definition in Eq. 6.

In the current application, we estimated the flushing time (T_f) for each grid cell by fitting an exponential function to the tracer concentration results derived from the model simulation. Thus, by definition, the flushing time, T_f, represents the time duration for the initial tracer concentration (C_0) to be reduced by a factor of e^{-1}, known as "e-folding time" (Dettmann, 2001), which corresponds to a ~63% decay in C_0. Using the methodology described above, we quantified flushing times at all grid cells inside the domain under various scenarios described below.

3.3.1. Tidal Variability Effect

Estuarine flushing time is highly influenced by the tidal range and phase (e.g., spring-neap variability), which controls the exchange of oceanic and embayed waters, particularly for low-inflow estuaries, where fluvial inflow/exchange is limited. In the current modeling application, we find that the tidal variability over the first several days of the simulation imposes a significant effect on the flushing time estimates. To evaluate the influence of the tidal range and phase (with respect to the spring-neap cycle) on the flushing time, we set the model to start at four different time instances representing four different tidal range conditions: a neap tide start (i.e., a model run that starts on Aug 3rd, 2018), a neap-to-spring transition start (Aug 7th), a spring tide start (Aug 11th), and a spring-to-neap transition start (Aug 14th). In all scenarios, the start time was selected so that the water level was close to the mean water level before a rising tide.

3.3.2. Bed Roughness Effect

Depth-averaged hydrodynamic models typically incorporate the effect of vegetation through an equivalent roughness coefficient near the bed, although this might neglect the three-dimensional influence of (possibly emergent) vegetation on the flow (Temmerman et al., 2005). Roughness coefficients, which approximate the physical resistance on the flow due to the seabed, are a source of uncertainty in hydrodynamic modeling and are usually considered a calibration parameter for the model (Warmink et al., 2007). By influencing the currents in tidally-dominated basins (Horstman et al., 2013), any alteration in the bed roughness via removal/growth of vegetation can alter (decrease/increase, respectively for removal/growth) local transport time scales (Kröger et al., 2009).

We utilized the (default) Chézy method for bed roughness in Delft3D, where its default value of $C = 65\ m^{\frac{1}{2}}s^{-1}$, as recommended by Warmink et al. (2007) for unlined earth beds, was selected for the model validation runs (since the default roughness demonstrates strong skill during the model calibration phase). This represents the post-eelgrass decline period when the field measurements also took place. To investigate the influence of eelgrass coverage on the local flushing times in the bay, the hydrodynamic model was run with varying bed roughness coefficient values lower than the default unlined earth value. These lower bed roughness coefficient values represent an increase in the effective bed roughness due to the presence of vegetation (i.e., seagrass), considering the inverse relationship between bed roughness and its coefficient for the Chézy method. Following Warmink et al. (2007), coefficient values of 35, 40, 45, and 50 $m^{\frac{1}{2}}s^{-1}$, were assigned to the intertidal areas mainly occupied by eelgrass prior to its major decline (e.g., areas in red color in the Fall 2007 subplot in Figure 1b). Here, the minimum applied bed roughness coefficient ($35\ m^{\frac{1}{2}}s^{-1}$) is the recommended value for fully vegetated beds and banks (Warmink et al., 2007). This range of coefficients also captures variations in eelgrass properties that modify drag at the bed (e.g., density, length, etc.). Differences in flushing time without vegetation ($C = 65\ m^{\frac{1}{2}}s^{-1}$) and with vegetation (35, 40, 45, and 50 $m^{\frac{1}{2}}s^{-1}$) were then quantified throughout Morro Bay. Here, a consistent neap-tide start was chosen for all runs to isolate the bed-roughness effect.

3.3.3. Sea-Level Rise Effect

In addition to strongly influencing tidal height, velocities, and hence exchange, water depth is a primary control on seagrass habitat suitability through its effect on both desiccation in the shallower range and light availability for photosynthesis in the deeper range (Duarte, 1991). We evaluated the effects of predicted sea-level rise over the upcoming decades on flushing-time estimates in Morro Bay and potential ecosystem impacts. We modeled different amounts of sea-level rise by adding these values to the local mean sea level (based on the National Tidal Datum Epoch, 1983-2001). We modeled three different sea-level rise scenarios of 10, 20, and 40 cm, which correspond to low-, medium, and high-end projections by 2050 based on the available spatiotemporally variable sea-level rise projections for this region (Kopp et al., 2014). We also evaluated a negative sea-level rise (-10 cm) for comparative purposes and to assess the impact of further erosion in the bay. The default bed roughness coefficient ($65\ m^{\frac{1}{2}}s^{-1}$) and a consistent neap-tide start was used for these simulations.

4. Results

4.1. Hydrodynamics Validation

The model skillfully reproduced the measured water levels, current velocities, and temperature at the four mooring locations during the study period. The model validation statistics across all sites are detailed in Table 1 and shown in Figures A1-A4 (see Appendix A). The simulated water level in Morro Bay is remarkably accurate and is dominated by the semi-diurnal tide and

displayed strong spring-neap variability with tidal ranges exceeding 2 m during spring tides (Figure A1). Depth-averaged velocities are also dominated by spring-neap variability, in phase quadrature with the water level. The magnitudes of the current velocity decrease going from the mouth to the head, and the current direction is generally aligned with the major axis of the channel (E-W at BM, and N-S at BC and BO). The model also showed excellent agreement with the observations, particularly for the major axis of flow (E-W or u-component at BM, and N-S or v component at BC and BO) (Table 1, Figures A2, A3). The minor axis component for the depth-averaged velocities (N-S or v-component at BM, and E-W or u-component at BC and BO), which generally represents the cross-channel velocities, was nearly an order of magnitude smaller than the major along-channel velocities and predominantly displayed good agreement with the observations (Table 1, Figures A2, A3). The lowest correlation value observed was in the cross-channel velocity at BM, albeit with minor errors, due to small differences in phasing (Figure A3a). The temperature was dominated by tidal variability with minimal lower-frequency variability (associated with variations in ambient air and ocean temperature applied via boundary conditions), both of which were accurately reproduced by the model across all sites (Table 1; Figure A4). Moreover, the model also satisfactorily reproduced the observed spatial gradients in temperature going from colder oceanic waters at the mouth to warmer temperatures in the back bay (driven by the heat flux to shallow waters). Overall, the model validation, particularly of advected temperature fields, lends confidence in its ability to predict the evolution of passive tracers for flushing time calculations.

Statistical measure	Monitoring station	Hydrodynamic parameter			
		Water level	U-Velocity	V-Velocity	Temperature
CC	BM	0.995	0.989	-0.350	0.851
	BC	0.991	0.856	0.926	0.882
	BO	0.993	0.863	0.977	0.841
	BS	0.994	–	–	0.810
$RMSE$	BM	0.04 m	0.09 m/s	0.06 m/s	0.83 ℃
	BC	0.07 m	0.08 m/s	0.10 m/s	0.88 ℃
	BO	0.06 m	0.02 m/s	0.06 m/s	1.03 ℃
	BS	0.05 m	–	–	1.02 ℃
$Skill$	BM	1	0.999	0.990	0.994
	BC	1	0.978	0.998	0.999
	BO	1	0.995	0.998	0.977
	BS	1	–	–	0.998

Table 1. *Statistical measures comparing the modeled hydrodynamic parameters to the observations at the monitoring stations*

4.2. Tidal Range and Release Time Effect on Flushing Time

Tidal variability over the first several days of the simulation imposes a significant effect on the flushing time estimates. The modeled tracer concentration at points within the bay generally displayed tidal fluctuations and an exponential decrease over longer time scales for all four initial tidal cycle starting points considered here (e.g., see station BO in Figure 3b, d, f, and h, with other locations in the domain displaying similar trends which are not shown here; the smoothed

curves are low-pass-filtered [using a 4th order Butterworth low-pass filter with a half-power frequency of 0.0005] tracer concentrations at station BO [C_{BO}]). The exponential decrease typically occurred following an initial lag of several days at BO, which is due to the incoming oceanic waters not yet reaching this location with the initial incoming tide and the lack of immediate mixing resembling a true CSTR system (see e.g., Delhez et al., 2004; Jouon et al., 2006; Monsen et al., 2002). To account for this, we adopted a concentration threshold for the tracer concentration ($C_1 = 0.99C_0$; see e.g., Jouon et al., 2006), such that when the tracer concentration in a grid cell reaches this threshold, the exponential fit is applied. The length of the shaded green rectangles in panels (b), (d), (f), and (h) in Figure 3 demonstrate the flushing time at station BO under each initial tidal scenario, where the tracer concentration decreases from the threshold concentration ($C_1 = 0.99C_0$) to the concentration corresponding to the e-folding time ($e^{-1}C_0 \approx 0.37C_0$), equivalent to the height of the shaded rectangles. For station BO, the flushing times under the various initial tidal scenarios are estimated as 4.57 days for the neap tide start, 6.17 days for the neap-to-spring start, 9.15 days for the spring tide start, and 8.26 days for the spring-to-neap start. As further discussed below, the flushing time is generally shorter during periods when the tide is ramping up (i.e., going from neap to spring) and longer when the tide is ramping down (i.e., going from spring to neap).

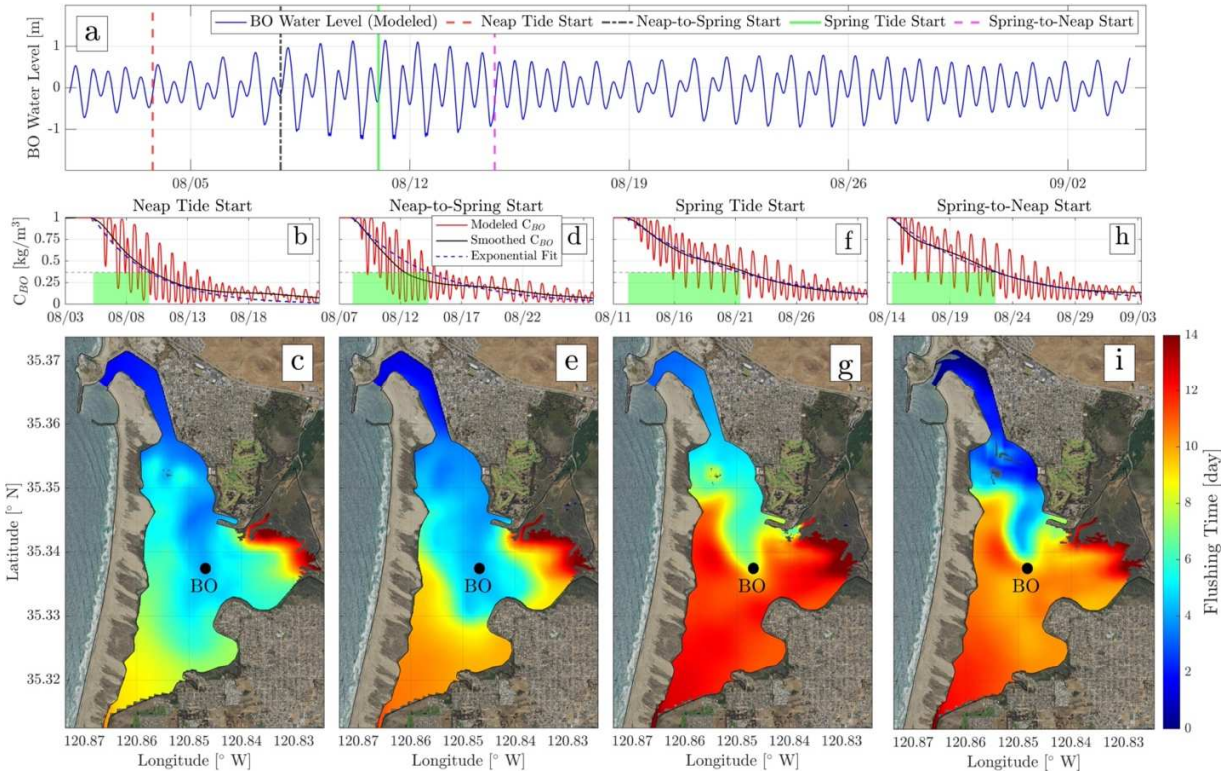

Figure 3. *(a) The modeled water levels at station BO during the simulation period, depicting the various start times (as initial tidal condition scenarios: neap tide start, neap-to-spring-start, spring tide start, and spring-to-neap start) used for the calculation of flushing times. Panels b, d, f, and h show the tracer concentration at station BO (in red), the smoothed (low-pass-filtered) tracer concentration (in black), and the exponential fit to the smoothed tracer concentration (in dashed blue). The length of the shaded green rectangle in each case corresponds to the calculated flushing time, with the height corresponding to the e-folding time concentration ($0.37C_0$). (c, e, g, and i) The local flushing times (in days) throughout the entire domain of the estuary under the different initial tidal conditions specified in panels b, d, f, and h, respectively.*

Examination of flushing times throughout Morro Bay revealed generally increasing flushing times with distance from the mouth, reaching up to 14 days in the back reaches of the estuary (Figure 3). Averaged across the domain, flushing time varies across the spring-neap cycle with 5.54, 6.36, 9.45, and 8.19 days, respectively, for the neap (Figure 3c), neap-to-spring (Figure 3e), spring (Figure 3g), and spring-to-neap (Figure 3i) starts. Tidal prism theory (see e.g., Monsen et al., 2002) states that increased tidal ranges will cause more flushing (i.e., decreased flushing times). The results presented here are broadly consistent with the notion that larger tides cause more flushing. However, because both the bulk flushing times and the 'quarter' of the moon phase are approximately one week long, the phasing of the spring-neap variability strongly affects the flushing time. The model simulations starting just before large spring tides generally experience the shortest flushing times (Figure 3b, d). On the other hand, when the model starts exactly on a spring tide (Figure 3f, h), the bay generally does not fully flush before the next neap cycle, in which exchange is more limited, resulting in longer flushing times. This behavior is also likely due to complex geometry and channelization across the back portions of the bay that deviate from an idealized model framework and drive increased flushing times with elevated tidal range start times. We found that the middle of the bay (e.g., near the location of BO) represents a fairly sharp transition between short flushing times near the mouth and long flushing times near the mid- to back-bay, where Morro Bay widens and the main channel becomes separated on both sides by tidal flats.

4.3. Bed Roughness Effect on Flushing Time

Increases in bed roughness (which corresponds to decreases in Chézy coefficients) increased flushing times throughout Morro Bay, with flushing times rising by nearly one day compared to the case of the default unvegetated bed roughness coefficient (Figure 4). In general, the higher the bed roughness (representing increased vegetation), the greater the flushing time relative to the unvegetated case (e.g., inverse relationship between bed roughness coefficient and flushing time estimates). Averaged across the domain, flushing times increased by 0.66, 0.58, 0.49, and 0.38 days, respectively, relative to the default Chézy bed roughness coefficient (65 $m^{\frac{1}{2}}s^{-1}$) for coefficients of 35, 40, 45, and 50 $m^{\frac{1}{2}}s^{-1}$ (e.g., decreasing effective bed roughness for increasing Chézy coefficients). Examining the spatial influence of increasing bed roughness, we found that locations in the northern areas of the bay near the mouth were unaffected by changing bed roughness. The central and southern areas of the bay, which encompass most of the regions of eelgrass loss (e.g., shaded areas in Figure 4), were the regions with increased flushing times (up to 1 day), with spatially similar increases in these regions.

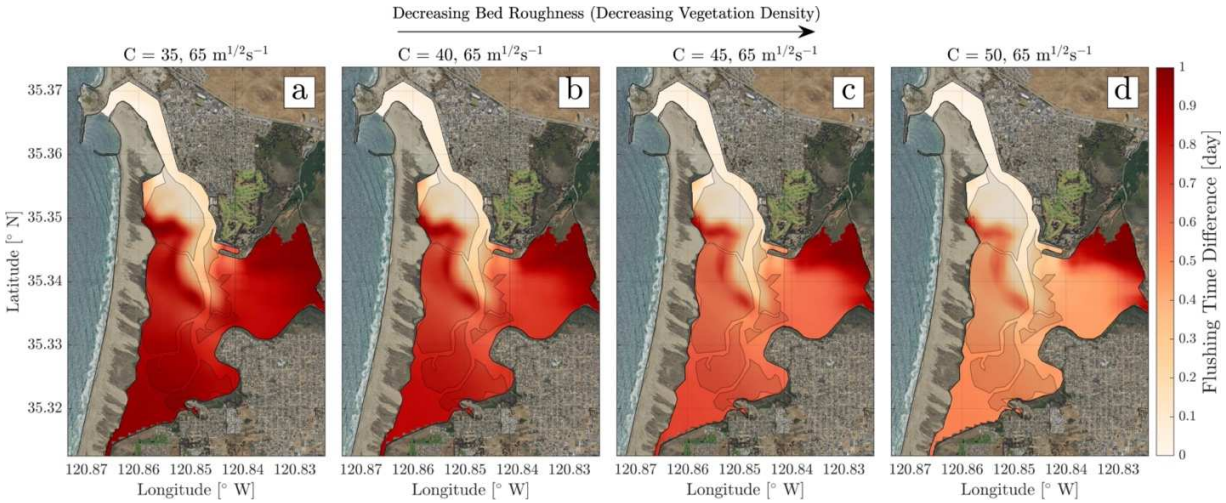

Figure 4. *Spatial distribution of the difference in flushing time between the decreased bed roughness coefficients of (a)* $C = 35\ m^{\frac{1}{2}}s^{-1}$*, (b)* $C = 40\ m^{\frac{1}{2}}s^{-1}$*, (c)* $C = 45\ m^{\frac{1}{2}}s^{-1}$*, and (d)* $C = 50\ m^{\frac{1}{2}}s^{-1}$*, respectively, and the base (unvegetated) case of* $C = 65\ m^{\frac{1}{2}}s^{-1}$*. The roughness coefficient was only changed in each case in the shaded regions, representing areas that were previously occupied by intertidal eelgrass, while the non-shaded areas kept the default coefficient of* $C = 65\ m^{\frac{1}{2}}s^{-1}$*.*

4.4. Sea-Level Rise Effect on Flushing Time

Sea-level rise decreased flushing times in Morro Bay by up to two days, while sea-level fall increased flushing times by up to two days (Figure 5). Averaged across the domain, the flushing time decreased by 0.51, 0.66, and 0.86 days for the 10, 20, and 40 cm sea-level rise scenarios, respectively, while it increased by 0.48 days for the negative (-10 cm) sea-level scenario. The impact of the sea-level rise on flushing time was most evident in the central and southern areas of Morro Bay, while the northern areas near the mouth were largely unaffected (similar to Section 4.3). The salt marsh located at the far eastern, central region of Morro Bay was most affected by changes in sea level. Sea-level rise has almost a negligible effect on the modeled tidal ranges in Morro Bay at all monitoring stations (e.g., a 0.2% increase in tidal ranges at BC, BO, and BS, respectively, and 0.07% at BM for the 40 cm sea-level rise scenario).

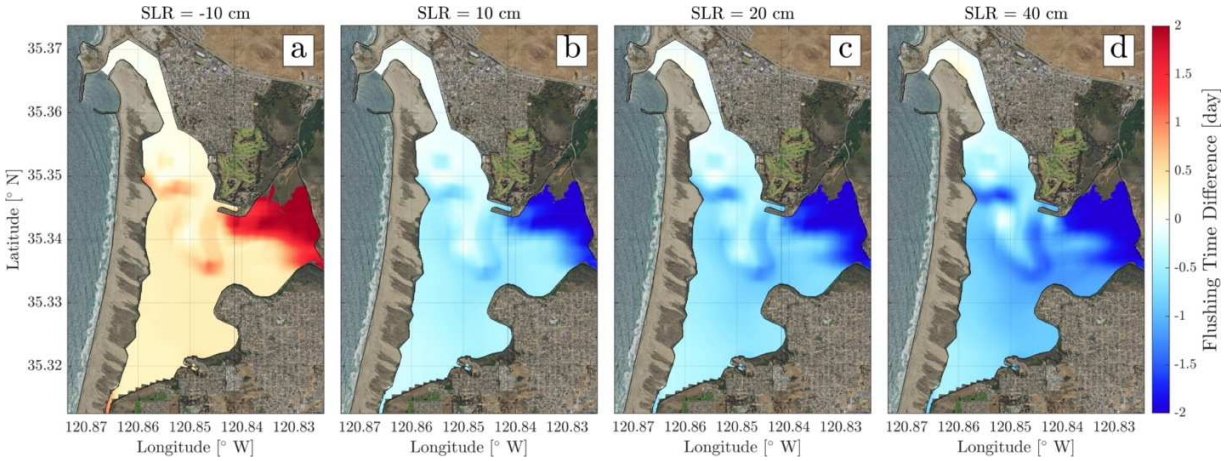

Figure 5. *Spatial distribution of the difference in flushing times between a sea-level rise of (a) -10 cm, (b) 10 cm, (c) 20 cm, and (d) 40 cm and current mean sea level (MSL = 0 cm).*

5. Discussion

Estuarine geometry (e.g., size and depth) and inflow conditions (e.g., tidally-driven oceanic exchange and freshwater input) strongly impact estuarine hydrodynamics, affecting flushing times, water quality, and estuarine ecology (Aiken, 2008; Ensing et al., 2015; Prandle, 2003; Talke & Jay, 2020). Classical estuaries with persistent freshwater inflow and enhanced gravitational circulation (see e.g., Largier, 2010; Largier et al., 1997; Nidzieko & Monismith, 2013) exhibit different hydrodynamic behavior than short LIEs like Morro Bay. Lacking freshwater inflow and gravitational circulation, the hydrodynamics of LIEs are strongly driven by tidal exchange with the ocean, which can be highly variable across daily, spring-neap, and longer nodal cycles (see e.g., Peng et al., 2019). Furthermore, short LIEs exhibit a unique sensitivity to varying hydrodynamic and flushing processes because the estuary-ocean exchange volume (e.g., tidal prism) represents a high percentage of the estuary's mean water volume (e.g., approximately on the order of 40-50% in Morro Bay). Consequently, short LIEs are highly sensitive to perturbations in exchange volume associated with tidal variability and sea-level rise. Additionally, the limited depth of many short LIEs enhances their sensitivity to changing bed-roughness effects (as shown here), which can be associated with changes in vegetation coverage due to seagrass, for instance.

Here we found estuarine flushing times are highly sensitive to the spring-neap variability, such that smaller tidal ranges (when averaged over 1-2 weeks) resulted in increased flushing times throughout the estuary, as consistent with tidal prism theory (cf. Monsen et al., 2002). The timing of tracer releases with respect to the tidal range (i.e., phasing with the spring-neap cycles) was the dominant driver of flushing time variability in our study, with up to 70% differences in flushing times associated with different tidal range start times (Table 2). We also found that an increase in effective bed roughness (e.g., an increase in vegetation or a decreasing Chézy bed roughness coefficient) resulted in increases in flushing time of around 10% when compared to the unvegetated base case (Table 2). Finally, the sea-level rise of up to 40 cm decreases in flushing time by around 10% when compared to the base case of no sea-level rise (Table 2). Spatially, flushing times near the mouth were relatively unaffected by changes to these

parameters, whereas changes in flushing time in the back bay were the most affected. Collectively, these results highlight the importance of considering the spatiotemporal variability of flushing time and contributions of individual processes, as opposed to bulk integrative methods (Monsen et al., 2002).

Tidal Variability Effect (Compared to the case with Neap Tide Start)	Initial Tidal Scenario	$\Delta T_{f_{avg}}$ (day)	$\Delta T_{f_{avg}}$ (%)
	Neap Tide	0	0.0
	Neap-to-Spring	0.82	14.8
	Spring Tide	3.91	70.6
	Spring-to-Neap	2.65	47.8
Bed Roughness Effect (Compared to the case with default bed roughness coefficient (C = 65 $m^{\frac{1}{2}}s^{-1}$) throughout the whole domain)	C ($m^{\frac{1}{2}}s^{-1}$)	$\Delta T_{f_{avg}}$ (day)	$\Delta T_{f_{avg}}$ (%)
	65	0	0
	35	0.66	11.9
	40	0.58	10.5
	45	0.49	8.8
	50	0.38	6.9
Sea-Level Rise Effect (Compared to the case with SLR = 0 cm)	SLR (cm)	$\Delta T_{f_{avg}}$ (day)	$\Delta T_{f_{avg}}$ (%)
	0	0	0
	-10	0.48	8.7
	10	-0.51	-9.2
	20	-0.66	-11.9
	40	-0.86	-15.5

Table 2. *The effect of tidal variability, bed roughness, and sea-level rise on the spatially-averaged flushing times ($T_{f_{avg}}$) throughout the domain*

Hydrodynamic control of exchange processes, water quality, and biological/ecological processes is further supported by observations that different portions of LIEs experience distinct water quality metrics, habitats, and ecosystems (Bartoloni et al., 2023; Buck et al., 2014; Largier et al., 1997; Walter et al., 2018). During the period of eelgrass decline in Morro Bay from 2007 to 2017, the mid- and back-bay areas experienced eelgrass loss while eelgrass in forebay areas persisted. Limited data on eelgrass condition and water quality during the period of decline makes it hard to establish clear causality. However, based on the results of this study and the strong spatial variations in flushing time in Morro Bay, it is possible that higher flushing times in the mid- and back-bay areas may have contributed to eelgrass loss since high flushing times can cause poor water quality conditions through biogeochemical modification (see e.g., Bartoloni et al., 2023; Walter et al., 2018).

Furthermore, the model showed that a decrease in effective bed roughness (due to loss of vegetation like eelgrass, for example) led to a decline in flushing times. This could potentially influence the dynamics in eelgrass ecosystems, whereby the local flushing time is modified back toward a range that improves water quality and supports eelgrass regrowth. However, this potential feedback loop requires further testing and may not be as important of a driver of

eelgrass dynamics compared to other well-documented feedback loops in seagrass systems like the seagrass-sediment-light feedback (Adams et al., 2016; Carr et al., 2010). Nonetheless, eelgrass in Morro Bay currently appears to be on a partial recovery trajectory in areas of the previous decline based on drone-based surveys over the last few years. The positive correlation between effective bed roughness and flushing time (e.g., an increase in bed roughness resulting in an increase in flushing times) potentially suggests that LIEs may be susceptible to cyclical changes in eelgrass (or other biogenic habitats) due to feedback loops between vegetation density and flushing time, however, this requires further testing. In Mediterranean climates where LIEs are common, supporting the resilience of biogenic habitats like eelgrass suggests that careful monitoring of short-term stressors (e.g., sedimentation) and long-term stressors (e.g., sea-level rise) may help to avoid putting these habitats over a tipping point leading to catastrophic decline or loss.

So far, no consensus has been established on how sea-level rise will influence flushing times in an estuary (Hong & Shen, 2012). The few studies (Du, 2017; Hong et al., 2020; Hong & Shen, 2012; Sullivan et al., 2020) that have investigated the relationship between sea-level rise and flushing times have returned inconsistent results where sea-level rise was found to increase, decrease, or not alter the flushing times significantly. We expect that the inconsistencies in flushing-time response to sea-level rise are due to the variation in estuarine geometry and processes across the various case studies. Short and shallow LIEs, however, represent a class of relatively simple estuarine systems in which flushing time is primarily dominated by the tidal exchange. Hence, it is clear that sea-level rise will generally increase the tidal prism in short LIEs, which will primarily increase exchange and secondarily reduce effective bottom drag (by increasing water depth), both of which should decrease flushing time (e.g., Du et al., 2018).

Uncertainties associated with the flushing times estimated here stem from various sources, some of which are more readily quantifiable than others. Uncertainties arising from the lack of observations in the shallower subtidal flats (due to the inherent limitations associated with in-situ monitoring equipment in these shallow regions that frequently wet and dry) and, consequently, lack of model calibration/validation in these areas are not quantifiable. Additionally, uncertainties originating from the ~1-year gap between the simulation and bathymetry data collection periods are not easily quantifiable either. On the other hand, the uncertainty associated with the use of the CSTR exponential decay model for the evolution of tracer concentration can be assessed. To characterize this uncertainty, we calculated the root-mean-square-difference ($RMSD$) between the flushing times calculated from the smoothed tracer concentration derived from the numerical model and that from the exponential decay fit to be 0.05, 0.09, 0.02, and 0.03 days for Neap Tide Start (Figure 3b), Neap-to-Spring-Start (Figure 3d), Spring Tide Start (Figure 3f), and Spring-to-Neap Start (Figure 3h) modes, respectively, for the BO station. These uncertainties are orders of magnitude smaller than the uncertainties stemming from the time selected for the release of the initial tracer concentration, where they cause up to ~4 days (~70%) of difference in the estimated average flushing time throughout Morro Bay (Table 2). Hence, the popular CSTR exponential decay model seems to provide a reasonably accurate representation of the time-averaged (e.g., low-pass filtered) tracer concentration within a tidally influenced estuary. However, there are two notable limitations of the CSTR exponential decay fit. First, unlike the time-averaged tracer concentration, the instantaneous tracer concentration field is highly oscillatory due to the tides (see panels (b), (d), (f), and (h) in Figure 3), and, thus, the

CSTR model is only suitable to describe the spatiotemporally averaged flushing behavior resulting from complex advection and diffusion processes. Second, applying an exponential fit to the time-averaged tracer concentration seems to be complicated by the quiescent period immediately after the start of the simulation (the length of the shaded purple rectangles in panels (b), (d), (f), and (h) in Figure B1 [see Appendix B]), where the tidal inflow of ocean waters at the mouth of the estuary has not yet reached the back-bay regions. This quiescent period is generally longer for simulations starting on neap tides and shorter for spring tides and could be included in the flushing time calculations (for example, see panels (c), (e), (g), and (i) in Figure B1). However, doing so generally does not change the primary finding that there is significant variability in flushing times depending on the tidal amplitude/phase. Although flushing time calculations are subject to many sources of uncertainty, the importance of tidal processes driving both hydrodynamics and flushing time dynamics in short, low-inflow estuaries remains apparent.

The results presented here highlight that the flushing time in short LIEs is highly sensitive to both natural (e.g., climate change-induced sea-level rise and changes in vegetation and bed roughness) and anthropogenic (e.g., alterations in morphology due to the periodic dredging of the bay mouth and habitat modification that alters the bed roughness) perturbations (see also discussion in Largier et al., 1997; Schettini et al., 2017; Walter et al., 2018). These perturbations vary considerably over a range of time scales and could also include seasonal and interannual variability in benthic habitat and vegetation that influence bed roughness, wet and dry years that lead to changes in low-inflow periods and exchange processes, natural climate oscillations (e.g., El Niño/Southern Oscillation and Pacific Decadal Oscillation) that modify the sea level, geomorphological changes to depth and estuarine geometry (and hence tidal variability) due to dredging and sediment loading from watershed influences, sea-level rise due to human accelerated climate change, and other short-term pulse stressors (episodic sediment loading events, etc.). Thus, flushing times in these systems are expected to vary substantially over a variety of short and long timescales, with the potential for nonlinear interactions and feedbacks between different system perturbations. It is possible that some LIEs may lack resilience to these disturbances since flushing times are highly sensitive to changes in physical drivers. Moreover, short LIEs may be more vulnerable to these perturbations compared to larger traditional (classical) estuaries since the hydrodynamic metrics directly affecting the flushing times are more susceptible to variability/perturbations in short LIEs (e.g., slight variations in tidal ranges causes significant percent variations in the tidal prism). Estuarine water quality and ecosystem health sensitivity to hydrodynamic perturbations and long-term pressures highlights the benefits of regular, proactive monitoring and management strategies of critical habitats in short low-inflow systems.

6. Conclusions

We developed a validated numerical model (Delft3D) to investigate the spatial variability of flushing times in Morro Bay, California, under the influence of various physical drivers, i.e., variability in tidal range, bed roughness, and sea level to investigate the potential impacts of flushing times, as a hydrodynamic metric influencing the water quality, on eelgrass health. Among these drivers, we found that the tidal range/phase was the dominant driver in flushing time variability, where increased tidal ranges enhanced the flushing times according to tidal prism theory. Moreover, there may be a feedback loop between flushing times and the effective

bed roughness, whereby a decrease in effective bed roughness (associated with loss of vegetation like eelgrass) lowers the local flushing times, potentially improving water quality conditions that support eelgrass health and regrowth, though further research is needed. Lastly, sea-level rise was found to lower flushing times due to the enhanced tidal prism and reduced effective bed roughness. Significant differences regarding how LIEs respond to these factors (in comparison with classic estuaries) emphasize that their unique geometric and hydrodynamic characteristics potentially expose them to be more susceptible to short- and long-term perturbations and stressors.

Acknowledgments

This publication was prepared under NOAA Grant #NA18OAR4170073, California Sea Grant College Program Project #R/HCE-07, through NOAA's National Sea Grant College Program, U.S. Department of Commerce. The statements, findings, conclusions, and recommendations are those of the authors and do not necessarily reflect the views of California Sea Grant, NOAA, or the U.S. Department of Commerce. We also acknowledge support from the NOAA IOOS through CeNCOOS for long-term data collected at BM and BS. R. Walter was supported by the Restore America's Estuaries Coastal Watersheds Grant. We thank the Morro Bay National Estuary Program for their longtime collaboration on studies in Morro Bay. We also acknowledge support in the field from Ian Robbins, Nicholas Trautman, Sydney Wewerka, Jason Felton, and Tom Moylan. Boating resources were provided by the Center for Coastal Marine Sciences.

Appendix A

Figures A1-A4, excluded from the main text body for brevity, demonstrate the time series of hydrodynamic processes in the Delft3D model (water level, current velocities, and temperature) validated against the observational data at the four monitoring stations during the simulation period.

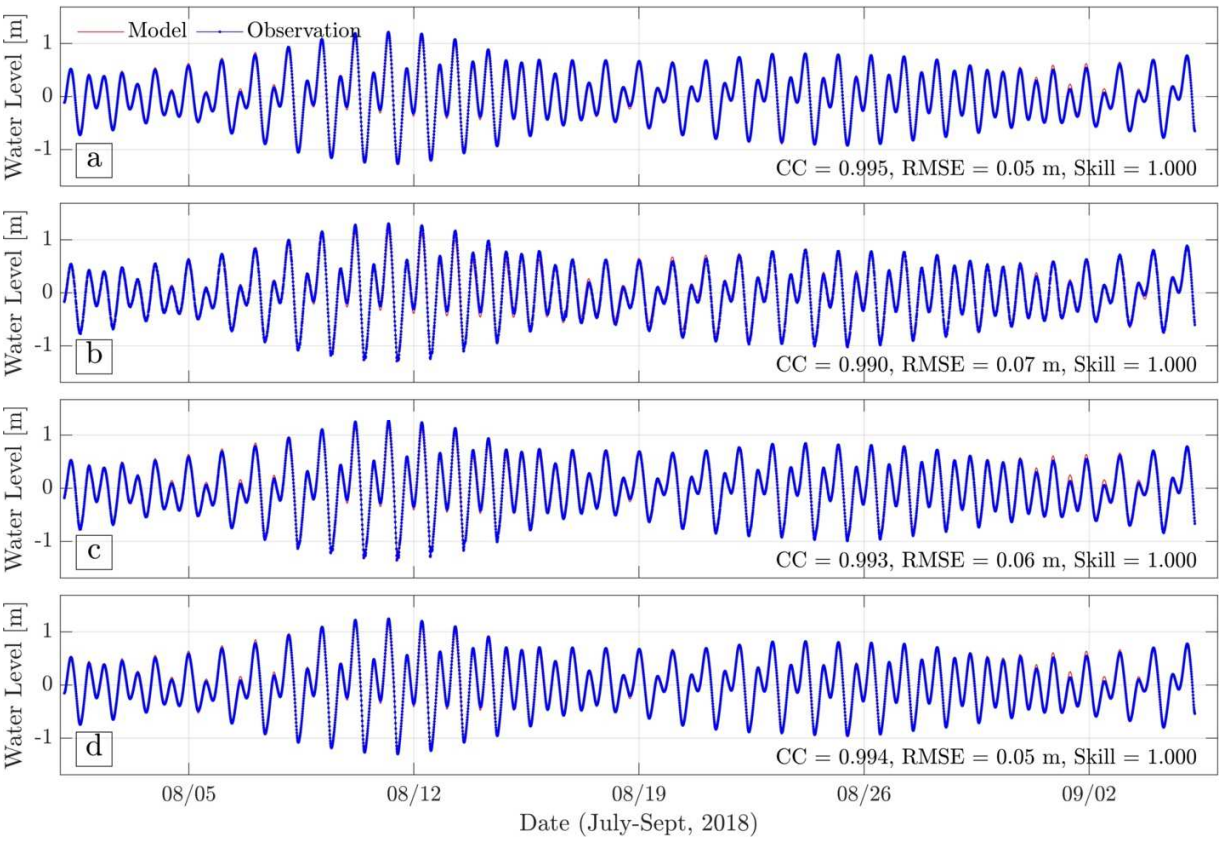

Figure A1. *Comparison between the modeled (red) and observed (blue) water levels (detrended) at monitoring stations (a) BM, (b) BC, (c) BO, and (d) BS. Error metrics are also shown in the bottom right corner of each plot.*

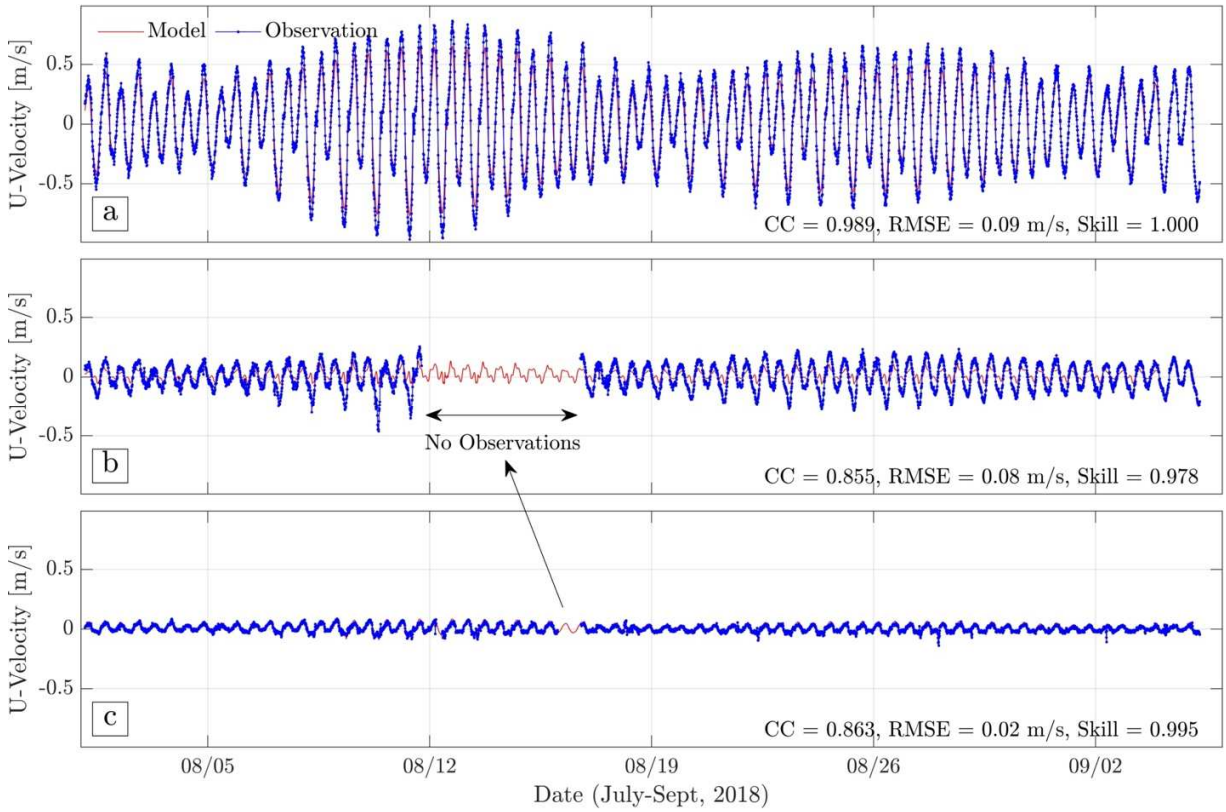

Figure A2. *Comparison between the modeled (red) and observed depth-averaged (blue) horizontal current velocities (u-component, denoting the east-west direction) at monitoring stations (a) BM, (b) BC, and (c) BO. Periods with no field observations were due to biofouling. No current meter was deployed at BS. Error metrics are also shown in the bottom right corner of each plot.*

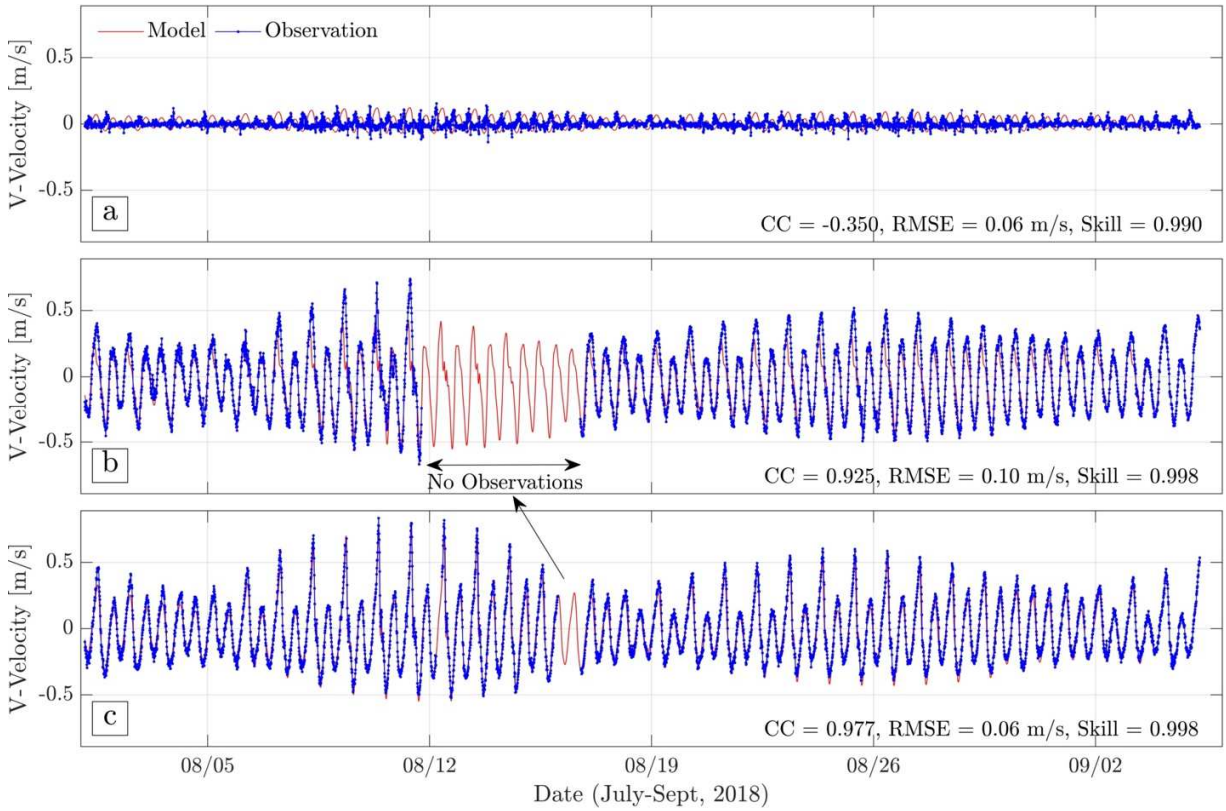

Figure A3. *Comparison between the modeled (red) and observed depth-averaged (blue) horizontal current velocities (v-component, denoting the north-south direction) at monitoring stations (a) BM, (b) BC, and (c) BO. Periods with no field observations were due to biofouling. No current meter was deployed at BS. Error metrics are also shown in the bottom right corner of each plot.*

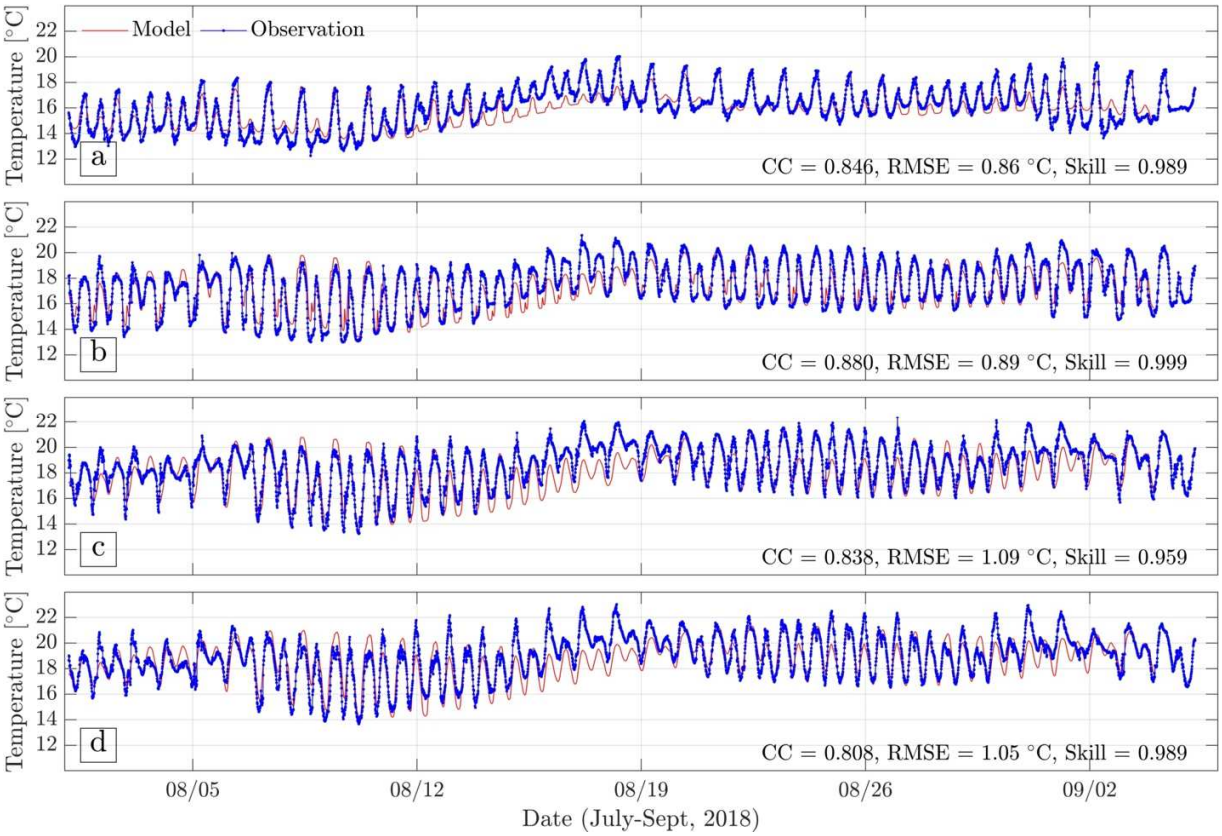

Figure A4. *Comparison between the modeled (red) and observed (blue) temperatures at monitoring stations (a) BM, (b) BC, (c) BO, and (d) BS. Error metrics are also shown in the bottom right corner of each plot.*

Appendix B

Figure B1 depicts the extended flushing times under four initial tide-phase scenarios (as described in sections 3.3.1 and 4.2), which includes the duration of the quiescent periods beginning from the start of the simulation up to where the tracer concentration reaches the threshold concentration $C_1 = 0.99C_0$. These extended flushing are generally ~1-5 days longer than the flushing times estimates shown in Figure 3 (with larger differences toward southern areas of the bay), but they exhibit similar spatial variability, as well as similar temporal variability related to the initial tide-phase scenarios.

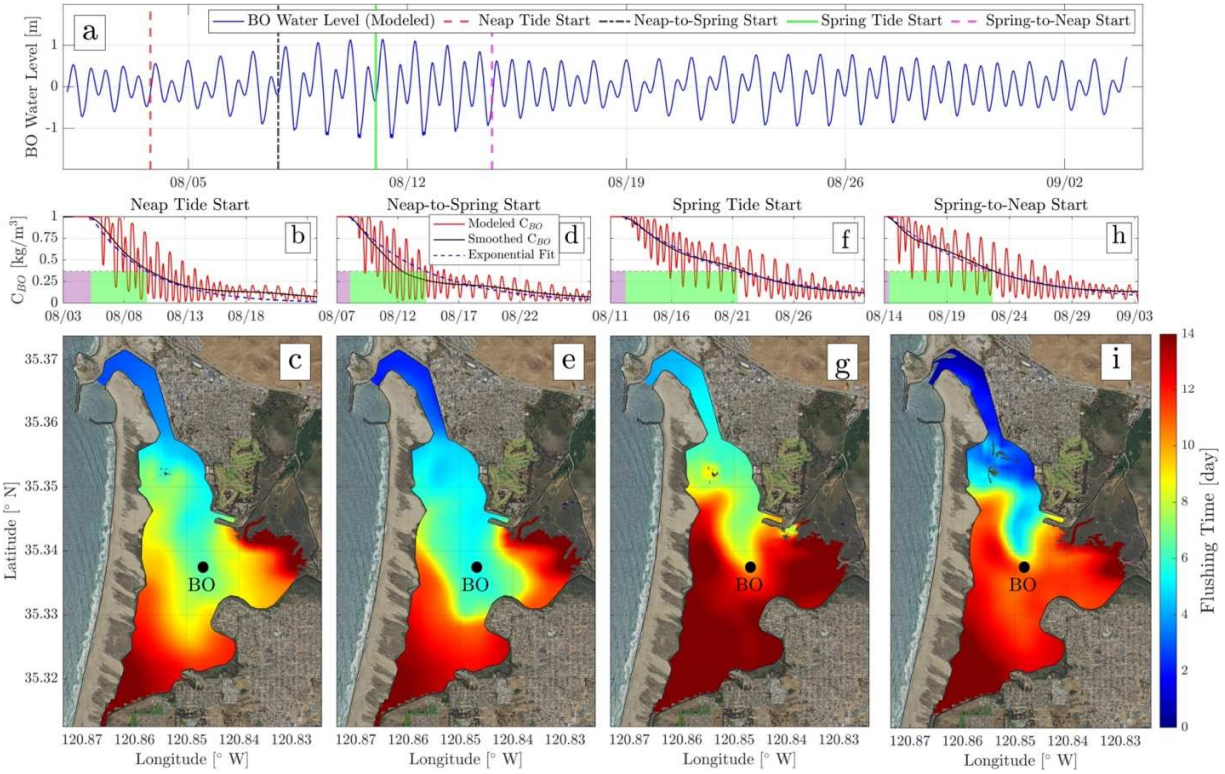

Figure B1. *(a) The modeled water levels at station BO during the simulation period, depicting the various start times (as initial tidal condition scenarios: neap tide start, neap-to-spring-start, spring tide start, and spring-to-neap start) used for the calculation of flushing times. Panels b, d, f, and h show the tracer concentration at station BO (in red), the smoothed (low-pass-filtered) tracer concentration (in black), and the exponential fit to the smoothed tracer concentration (in dashed blue). The sum of the lengths of the shaded green and purple rectangles in each case corresponds to the calculated extended flushing time, with the height corresponding to the e-folding time concentration ($0.37C_0$). (c, e, g, and i) The local extended flushing times (in days) throughout the entire domain of the estuary under the different initial tidal conditions specified in panels b, d, f, and h, respectively.*

References

Adams, M. P., Hovey, R. K., Hipsey, M. R., Bruce, L. C., Ghisalberti, M., Lowe, R. J., Gruber, R. K., Ruiz-Montoya, L., Maxwell, P. S., Callaghan, D. P., Kendrick, G. A., & O'Brien, K. R. (2016). Feedback between sediment and light for seagrass: Where is it important? *Limnology and Oceanography*, *61*(6), 1937–1955. https://doi.org/10.1002/lno.10319

Aiken, C. M. (2008). Barotropic tides of the Chilean Inland Sea and their sensitivity to basin geometry. *Journal of Geophysical Research: Oceans*, *113*(C8). https://doi.org/10.1029/2007JC004593

Al-Asadi, K., & Duan, J. G. (2017). Assessing methods for estimating roughness coefficient in a vegetated marsh area using Delft3D. *Journal of Hydroinformatics*, *19*(5), 766–783. https://doi.org/10.2166/hydro.2017.064

Andutta, F. P., Helfer, F., de Miranda, L. B., Deleersnijder, E., Thomas, C., & Lemckert, C. (2016). An assessment of transport timescales and return coefficient in adjacent tropical estuaries. *Continental Shelf Research*, *124*, 49–62. https://doi.org/10.1016/j.csr.2016.05.006

Andutta, F. P., Ridd, P. V., & Wolanski, E. (2013). The age and the flushing time of the Great Barrier Reef waters. *Continental Shelf Research*, *53*, 11–19. https://doi.org/10.1016/j.csr.2012.11.016

Barnard, P. L., van Ormondt, M., Erikson, L. H., Eshleman, J., Hapke, C., Ruggiero, P., Adams, P. N., & Foxgrover, A. C. (2014). Development of the Coastal Storm Modeling System (CoSMoS) for predicting the impact of storms on high-energy, active-margin coasts. *Natural Hazards*, *74*(2), 1095–1125. https://doi.org/10.1007/s11069-014-1236-y

Bartoloni, S. E., Walter, R. K., Wewerka, S. N., Higgins, J., O'Leary, J. K., & Bockmon, E. E. (2023). Spatial distribution of seawater carbonate chemistry and hydrodynamic controls in a low-inflow estuary. *Estuarine, Coastal and Shelf Science*, *281*, 108195. https://doi.org/10.1016/j.ecss.2022.108195

Buck, C. M., Wilkerson, F. P., Parker, A. E., & Dugdale, R. C. (2014). The Influence of Coastal Nutrients on Phytoplankton Productivity in a Shallow Low Inflow Estuary, Drakes Estero, California (USA). *Estuaries and Coasts*, *37*(4), 847–863. https://doi.org/10.1007/s12237-013-9737-6

Carr, J., D'Odorico, P., McGlathery, K., & Wiberg, P. (2010). Stability and bistability of seagrass ecosystems in shallow coastal lagoons: Role of feedbacks with sediment resuspension and light attenuation. *Journal of Geophysical Research: Biogeosciences*, *115*(G3). https://doi.org/10.1029/2009JG001103

Christensen, A., Twilley, R. R., Willson, C. S., & Castañeda-Moya, E. (2020). Simulating hydrological connectivity and water age within a coastal deltaic floodplain of the

831 Mississippi River Delta. *Estuarine, Coastal and Shelf Science*, *245*, 106995.
832 https://doi.org/10.1016/j.ecss.2020.106995

833 Cucco, A., Umgiesser, G., Ferrarin, C., Perilli, A., Canu, D. M., & Solidoro, C. (2009). Eulerian
834 and lagrangian transport time scales of a tidal active coastal basin. *Ecological Modelling*,
835 *220*(7), 913–922. https://doi.org/10.1016/j.ecolmodel.2009.01.008

836 Defne, Z., & Ganju, N. K. (2015). Quantifying the Residence Time and Flushing Characteristics
837 of a Shallow, Back-Barrier Estuary: Application of Hydrodynamic and Particle Tracking
838 Models. *Estuaries and Coasts*, *38*(5), 1719–1734. https://doi.org/10.1007/s12237-014-
839 9885-3

840 Delhez, É. J. M., Heemink, A. W., & Deleersnijder, É. (2004). Residence time in a semi-
841 enclosed domain from the solution of an adjoint problem. *Estuarine, Coastal and Shelf*
842 *Science*, *61*(4), 691–702. https://doi.org/10.1016/j.ecss.2004.07.013

843 den Heyer, C., & Kalff, J. (1998). Organic matter mineralization rates in sediments: A within-
844 and among-lake study. *Limnology and Oceanography*, *43*(4), 695–705.
845 https://doi.org/10.4319/lo.1998.43.4.0695

846 Dettmann, E. H. (2001). Effect of water residence time on annual export and denitrification of
847 nitrogen in estuaries: A model analysis. *Estuaries*, *24*(4), 481–490.
848 https://doi.org/10.2307/1353250

849 Dijkstra, J. T., & Uittenbogaard, R. E. (2010). Modeling the interaction between flow and highly
850 flexible aquatic vegetation. *Water Resources Research*, *46*(12).
851 https://doi.org/10.1029/2010WR009246

852 Drouzy, M., Douillet, P., Fernandez, J.-M., & Pinazo, C. (2019). Hydrodynamic time parameters
853 response to meteorological and physical forcings: Toward a stagnation risk assessment
854 device in coastal areas. *Ocean Dynamics*, *69*(8), 967–987.
855 https://doi.org/10.1007/s10236-019-01283-1

856 Du, J. (2017). Impact of Climate Variation and Human Adaptation on the Physical Transport
857 Processes and Water Exchange in Chesapeake Bay [Ph.D., The College of William and
858 Mary]. In *ProQuest Dissertations and Theses*. http://dx.doi.org/doi:10.21220/V5DN0N

859 Du, J., Shen, J., Zhang, Y. J., Ye, F., Liu, Z., Wang, Z., Wang, Y. P., Yu, X., Sisson, M., &
860 Wang, H. V. (2018). Tidal Response to Sea-Level Rise in Different Types of Estuaries:
861 The Importance of Length, Bathymetry, and Geometry. *Geophysical Research Letters*,
862 *45*(1), 227–235. https://doi.org/10.1002/2017GL075963

863 Duarte, C. M. (1991). Seagrass depth limits. *Aquatic Botany*, *40*(4), 363–377.
864 https://doi.org/10.1016/0304-3770(91)90081-F

865 Egbert, G. D., & Erofeeva, S. Y. (2002). Efficient Inverse Modeling of Barotropic Ocean Tides.
866 *Journal of Atmospheric and Oceanic Technology*, *19*(2), 183–204.
867 https://doi.org/10.1175/1520-0426(2002)019<0183:EIMOBO>2.0.CO;2

868 Ensing, E., de Swart, H. E., & Schuttelaars, H. M. (2015). Sensitivity of tidal motion in well-
869 mixed estuaries to cross-sectional shape, deepening, and sea level rise. *Ocean Dynamics*,
870 *65*(7), 933–950. https://doi.org/10.1007/s10236-015-0844-8

871 Hamilton, S. K., & Lewis Jr., W. M. (1987). Causes of seasonality in the chemistry of a lake on
872 the Orinoco River floodplain, Venezuela1. *Limnology and Oceanography*, *32*(6), 1277–
873 1290. https://doi.org/10.4319/lo.1987.32.6.1277

874 Harenčár, J. G., Lutgen, G. A., Taylor, Z. M., Saarman, N. P., & Yost, J. M. (2018). How
875 Population Decline Can Impact Genetic Diversity: A Case Study of Eelgrass (Zostera
876 marina) in Morro Bay, California. *Estuaries and Coasts*, *41*(8), 2356–2367.
877 https://doi.org/10.1007/s12237-018-0421-8

878 Hinrichs, C., Flagg, C. N., & Wilson, R. E. (2018). Great South Bay After Sandy: Changes in
879 Circulation and Flushing due to New Inlet. *Estuaries and Coasts*, *41*(8), 2172–2190.
880 https://doi.org/10.1007/s12237-018-0423-6

881 Holleman, R. C., & Stacey, M. T. (2014). Coupling of Sea Level Rise, Tidal Amplification, and
882 Inundation. *Journal of Physical Oceanography*, *44*(5), 1439–1455.
883 https://doi.org/10.1175/JPO-D-13-0214.1

884 Hong, B., & Shen, J. (2012). Responses of estuarine salinity and transport processes to potential
885 future sea-level rise in the Chesapeake Bay. *Estuarine, Coastal and Shelf Science*, *104–*
886 *105*, 33–45. https://doi.org/10.1016/j.ecss.2012.03.014

887 Hong, B., Liu, Z., Shen, J., Wu, H., Gong, W., Xu, H., & Wang, D. (2020). Potential physical
888 impacts of sea-level rise on the Pearl River Estuary, China. *Journal of Marine Systems*,
889 *201*, 103245. https://doi.org/10.1016/j.jmarsys.2019.103245

890 Horstman, E., Dohmen-Janssen, M., & Hulscher, S. (2013). Modeling tidal dynamics in a
891 mangrove creek catchment in Delft3D. *Coastal Dynamics*, 12.

892 Huggett, R. D., Purdie, D. A., & Haigh, I. D. (2021). Modelling the Influence of Riverine Inputs
893 on the Circulation and Flushing Times of Small Shallow Estuaries. *Estuaries and Coasts*,
894 *44*(1), 54–69. https://doi.org/10.1007/s12237-020-00776-3

895 Jiang, L., Soetaert, K., & Gerkema, T. (2019). Decomposing the intra-annual variability of
896 flushing characteristics in a tidal bay along the North Sea. *Journal of Sea Research*, *155*,
897 101821. https://doi.org/10.1016/j.seares.2019.101821

898 Josefson, A. B., & Rasmussen, B. (2000). Nutrient Retention by Benthic Macrofaunal Biomass
899 of Danish Estuaries: Importance of Nutrient Load and Residence Time. *Estuarine,*
900 *Coastal and Shelf Science*, *50*(2), 205–216. https://doi.org/10.1006/ecss.1999.0562

901 Jouon, A., Douillet, P., Ouillon, S., & Fraunié, P. (2006). Calculations of hydrodynamic time
902 parameters in a semi-opened coastal zone using a 3D hydrodynamic model. *Continental*
903 *Shelf Research*, *26*(12), 1395–1415. https://doi.org/10.1016/j.csr.2005.11.014

Khojasteh, D., Glamore, W., Heimhuber, V., & Felder, S. (2021). Sea level rise impacts on estuarine dynamics: A review. *Science of The Total Environment*, *780*, 146470. https://doi.org/10.1016/j.scitotenv.2021.146470

Kobashi, D., & Mazda, Y. (2005). Tidal Flow in Riverine-Type Mangroves. *Wetlands Ecology and Management*, *13*(6), 615–619. https://doi.org/10.1007/s11273-004-3481-4

Kopp, R. E., Horton, R. M., Little, C. M., Mitrovica, J. X., Oppenheimer, M., Rasmussen, D. J., Strauss, B. H., & Tebaldi, C. (2014). Probabilistic 21st and 22nd century sea-level projections at a global network of tide-gauge sites. *Earth's Future*, *2*(8), 383–406. https://doi.org/10.1002/2014EF000239

Kröger, R., Moore, M. T., Locke, M. A., Cullum, R. F., Steinriede, R. W., Testa, S., Bryant, C. T., & Cooper, C. M. (2009). Evaluating the influence of wetland vegetation on chemical residence time in Mississippi Delta drainage ditches. *Agricultural Water Management*, *96*(7), 1175–1179. https://doi.org/10.1016/j.agwat.2009.03.002

Lacy, J. R., & Wyllie-Echeverria, S. (2011). The influence of current speed and vegetation density on flow structure in two macrotidal eelgrass canopies. *Limnology and Oceanography: Fluids and Environments*, *1*(1), 38–55. https://doi.org/10.1215/21573698-1152489

Largier, J. (2010). Low-inflow estuaries: Hypersaline, inverse, and thermal scenarios. In A. Valle-Levinson (Ed.), *Contemporary Issues in Estuarine Physics* (pp. 247–272). Cambridge University Press. https://doi.org/10.1017/CBO9780511676567.010

Largier, J. L., Hollibaugh, J. T., & Smith, S. V. (1997). Seasonally Hypersaline Estuaries in Mediterranean-climate Regions. *Estuarine, Coastal and Shelf Science*, *45*(6), 789–797. https://doi.org/10.1006/ecss.1997.0279

Leijnse, T., van Ormondt, M., Nederhoff, K., & van Dongeren, A. (2021). Modeling compound flooding in coastal systems using a computationally efficient reduced-physics solver: Including fluvial, pluvial, tidal, wind- and wave-driven processes. *Coastal Engineering*, *163*, 103796. https://doi.org/10.1016/j.coastaleng.2020.103796

Lencart e Silva, J. D., Lopes, C. L., Picado, A., Sousa, M. C., & Dias, J. M. (2014). Tidal dispersion and flushing times in a multiple inlet lagoon. *Journal of Coastal Research*, *70 (10070)*, 598–603. https://doi.org/10.2112/SI70-101.1

Lesser, G. R., Roelvink, J. A., van Kester, J. A. T. M., & Stelling, G. S. (2004). Development and validation of a three-dimensional morphological model. *Coastal Engineering*, *51*(8), 883–915. https://doi.org/10.1016/j.coastaleng.2004.07.014

Lucas, L. V., & Deleersnijder, E. (2020). Timescale Methods for Simplifying, Understanding and Modeling Biophysical and Water Quality Processes in Coastal Aquatic Ecosystems: A Review. *Water*, *12*(10), 2717. https://doi.org/10.3390/w12102717

940 Luhar, M., & Nepf, H. M. (2013). From the blade scale to the reach scale: A characterization of
941 aquatic vegetative drag. *Advances in Water Resources*, *51*, 305–316.
942 https://doi.org/10.1016/j.advwatres.2012.02.002

943 Luhar, M., Coutu, S., Infantes, E., Fox, S., & Nepf, H. (2010). Wave-induced velocities inside a
944 model seagrass bed. *Journal of Geophysical Research: Oceans*, *115*(C12).
945 https://doi.org/10.1029/2010JC006345

946 MacCready, P., & Geyer, W. (2010). Advances in Estuarine Physics. *Annual Review of Marine*
947 *Science*, *2*, 35–58. https://doi.org/10.1146/annurev-marine-120308-081015

948 Mahanty, M. M., Mohanty, P. K., Pattnaik, A. K., Panda, U. S., Pradhan, S., & Samal, R. N.
949 (2016). Hydrodynamics, temperature/salinity variability and residence time in the Chilika
950 lagoon during dry and wet period: Measurement and modeling. *Continental Shelf*
951 *Research*, *125*, 28–43. https://doi.org/10.1016/j.csr.2016.06.017

952 Mariotti, G., & Murshid, S. (2018). A 2D Tide-Averaged Model for the Long-Term Evolution of
953 an Idealized Tidal Basin-Inlet-Delta System. *Journal of Marine Science and Engineering*,
954 *6*(4), 154. https://doi.org/10.3390/jmse6040154

955 Marsooli, R., Orton, P. M., Fitzpatrick, J., & Smith, H. (2018). Residence Time of a Highly
956 Urbanized Estuary: Jamaica Bay, New York. *Journal of Marine Science and*
957 *Engineering*, *6*(2), 44. https://doi.org/10.3390/jmse6020044

958 McDonald, C. B., Koseff, J. R., & Monismith, S. G. (2006). Effects of the depth to coral height
959 ratio on drag coefficients for unidirectional flow over coral. *Limnology and*
960 *Oceanography*, *51*(3), 1294–1301. https://doi.org/10.4319/lo.2006.51.3.1294

961 Monismith, S. G., Hirsh, H., Batista, N., Francis, H., Egan, G., & Dunbar, R. B. (2019). Flow
962 and Drag in a Seagrass Bed. *Journal of Geophysical Research: Oceans*, *124*(3), 2153–
963 2163. https://doi.org/10.1029/2018JC014862

964 Monsen, N. E., Cloern, J. E., Lucas, L. V., & Monismith, S. G. (2002). A comment on the use of
965 flushing time, residence time, and age as transport time scales. *Limnology and*
966 *Oceanography*, *47*(5), 1545–1553. https://doi.org/10.4319/lo.2002.47.5.1545

967 Nepf, H. M. (2012). Hydrodynamics of vegetated channels. *Journal of Hydraulic Research*,
968 *50*(3), 262–279. https://doi.org/10.1080/00221686.2012.696559

969 Nidzieko, N. J., & Monismith, S. G. (2013). Contrasting Seasonal and Fortnightly Variations in
970 the Circulation of a Seasonally Inverse Estuary, Elkhorn Slough, California. *Estuaries*
971 *and Coasts*, *36*(1), 1–17. https://doi.org/10.1007/s12237-012-9548-1

972 Nixon, S. W., Ammerman, J. W., Atkinson, L. P., Berounsky, V. M., Billen, G., Boicourt, W. C.,
973 Boynton, W. R., Church, T. M., Ditoro, D. M., Elmgren, R., Garber, J. H., Giblin, A. E.,
974 Jahnke, R. A., Owens, N. J. P., Pilson, M. E. Q., & Seitzinger, S. P. (1996). The fate of
975 nitrogen and phosphorus at the land-sea margin of the North Atlantic Ocean.
976 *Biogeochemistry*, *35*(1), 141–180. https://doi.org/10.1007/BF02179826

977 O'Leary, J. K., Goodman, M. C., Walter, R. K., Willits, K., Pondella, D. J., & Stephens, J.
978 (2021). Effects of Estuary-Wide Seagrass Loss on Fish Populations. *Estuaries and*
979 *Coasts*, *44*(8), 2250–2264. https://doi.org/10.1007/s12237-021-00917-2

980 Palazzoli, I., Leonardi, N., Jiménez-Robles, A. M., & Fagherazzi, S. (2020). Velocity skew
981 controls the flushing of a tracer in a system of shallow bays with multiple inlets.
982 *Continental Shelf Research*, *192*, 104008. https://doi.org/10.1016/j.csr.2019.104008

983 Peng, D., Hill, E. M., Meltzner, A. J., & Switzer, A. D. (2019). Tide Gauge Records Show That
984 the 18.61-Year Nodal Tidal Cycle Can Change High Water Levels by up to 30 cm.
985 *Journal of Geophysical Research: Oceans*, *124*(1), 736–749.
986 https://doi.org/10.1029/2018JC014695

987 Pokavanich, T., & Alosairi, Y. (2014). Summer Flushing Characteristics of Kuwait Bay. *Journal*
988 *of Coastal Research*, *30*(5), 1066–1073. https://doi.org/10.2112/JCOASTRES-D-13-
989 00188.1

990 Prandle, D. (2003). Relationships between Tidal Dynamics and Bathymetry in Strongly
991 Convergent Estuaries. *Journal of Physical Oceanography*, *33*(12), 2738–2750.
992 https://doi.org/10.1175/1520-0485(2003)033<2738:RBTDAB>2.0.CO;2

993 Ralston, D. K., Talke, S., Geyer, W. R., Al-Zubaidi, H. A. M., & Sommerfield, C. K. (2019).
994 Bigger Tides, Less Flooding: Effects of Dredging on Barotropic Dynamics in a Highly
995 Modified Estuary. *Journal of Geophysical Research: Oceans*, *124*(1), 196–211.
996 https://doi.org/10.1029/2018JC014313

997 Roelvink, J. A., & Banning, G. K. F. M. V. (1995). Design and development of DELFT3D and
998 application to coastal morphodynamics. *Oceanographic Literature Review*, *11*(42), 925.

999 Rynne, P., Reniers, A., van de Kreeke, J., & MacMahan, J. (2016). The effect of tidal exchange
1000 on residence time in a coastal embayment. *Estuarine, Coastal and Shelf Science*, *172*,
1001 108–120. https://doi.org/10.1016/j.ecss.2016.02.001

1002 Sanford, L. P., Boicourt, W. C., & Rives, S. R. (1992). Model for Estimating Tidal Flushing of
1003 Small Embayments. *Journal of Waterway, Port, Coastal, and Ocean Engineering*,
1004 *118*(6), 635–654. https://doi.org/10.1061/(ASCE)0733-950X(1992)118:6(635)

1005 Schettini, C. A. F., Valle-Levinson, A., & Truccolo, E. C. (2017). Circulation and transport in
1006 short, low-inflow estuaries under anthropogenic stresses. *Regional Studies in Marine*
1007 *Science*, *10*, 52–64. https://doi.org/10.1016/j.rsma.2017.01.004

1008 Sinha, P. C., Rao, Y. R., Dube, S. K., & Murty, T. S. (1997). Effect of sea level rise on tidal
1009 circulation in the Hooghly Estuary, Bay of Bengal. *Marine Geodesy*, *20*(4), 341–366.
1010 https://doi.org/10.1080/01490419709388114

1011 Sullivan, J. C., Wan, Y., & Willis, R. A. (2020). Modeling Floodplain Inundation, Circulation,
1012 and Residence Time Under Changing Tide and Sea Levels. *Estuaries and Coasts*, *43*(4),
1013 693–707. https://doi.org/10.1007/s12237-020-00709-0

Sweers, H. E. (1976). A nomogram to estimate the heat-exchange coefficient at the air-water interface as a function of wind speed and temperature; a critical survey of some literature. *Journal of Hydrology*, *30*, 375–401. https://doi.org/10.1016/0022-1694(76)90120-7

Takeoka, H. (1984). Fundamental concepts of exchange and transport time scales in a coastal sea. *Continental Shelf Research*, *3*(3), 311–326. https://doi.org/10.1016/0278-4343(84)90014-1

Talke, S. A., & Jay, D. A. (2020). Changing Tides: The Role of Natural and Anthropogenic Factors. *Annual Review of Marine Science*, *12*(1), 121–151. https://doi.org/10.1146/annurev-marine-010419-010727

Taylor, K. E. (2001). Summarizing multiple aspects of model performance in a single diagram. *Journal of Geophysical Research: Atmospheres*, *106*(D7), 7183–7192. https://doi.org/10.1029/2000JD900719

Temmerman, S., Bouma, T. J., Govers, G., Wang, Z. B., De Vries, M. B., & Herman, P. M. J. (2005). Impact of vegetation on flow routing and sedimentation patterns: Three-dimensional modeling for a tidal marsh. *Journal of Geophysical Research: Earth Surface*, *110*(F4). https://doi.org/10.1029/2005JF000301

Walter, R. K., O'Leary, J. K., Vitousek, S., Taherkhani, M., Geraghty, C., & Kitajima, A. (2020). Large-scale erosion driven by intertidal eelgrass loss in an estuarine environment. *Estuarine, Coastal and Shelf Science*, *243*, 106910. https://doi.org/10.1016/j.ecss.2020.106910

Walter, R. K., Rainville, E. J., & O'Leary, J. K. (2018). Hydrodynamics in a shallow seasonally low-inflow estuary following eelgrass collapse. *Estuarine, Coastal and Shelf Science*, *213*, 160–175. https://doi.org/10.1016/j.ecss.2018.08.026

Warmink, J. J., Booij, M. J., Van der Klis, H., & Hulscher, S. (2007). Uncertainty in water level predictions due to various calibrations. *Proc. of CAIWA*, 1–18.

Waycott, M., Duarte, C. M., Carruthers, T. J. B., Orth, R. J., Dennison, W. C., Olyarnik, S., Calladine, A., Fourqurean, J. W., Heck, K. L., Hughes, A. R., Kendrick, G. A., Kenworthy, W. J., Short, F. T., & Williams, S. L. (2009). Accelerating loss of seagrasses across the globe threatens coastal ecosystems. *Proceedings of the National Academy of Sciences*, *106*(30), 12377–12381. https://doi.org/10.1073/pnas.0905620106

Willmott, C. J. (1981). On the Validation of Models. *Physical Geography*, *2*(2), 184–194. https://doi.org/10.1080/02723646.1981.10642213

Wilson, J. R., Wilkerson, F. P., Blaser, S. B., & Nielsen, K. J. (2021). Phytoplankton Community Structure in a Seasonal Low-Inflow Estuary Adjacent to Coastal Upwelling (Drakes Estero, CA, USA). *Estuaries and Coasts*, *44*(3), 769–787. https://doi.org/10.1007/s12237-020-00792-3

1050 Xiong, J., Shen, J., Qin, Q., & Du, J. (2021). Water exchange and its relationships with external
1051 forcings and residence time in Chesapeake Bay. *Journal of Marine Systems*, *215*, 103497.
1052 https://doi.org/10.1016/j.jmarsys.2020.103497

1053 Zhong, L., Li, M., & Foreman, M. G. G. (2008). Resonance and sea level variability in
1054 Chesapeake Bay. *Continental Shelf Research*, *28*(18), 2565–2573.
1055 https://doi.org/10.1016/j.csr.2008.07.007